Applied Physics Letters

RESEARCH ARTICLE | JULY 18 2023

Efficient charge to spin conversion in iridium oxide thin films

Biswajit Sahoo ; Alex Frano ; Eric. E. Fullerton

Appl. Phys. Lett. 123, 032404 (2023)
https://doi.org/10.1063/5.0153329
CHORUS

AIP Publishing

Applied Physics Letters ARTICLE pubs.aip.org/aip/apl

Efficient charge to spin conversion in iridium oxide thin films

Cite as: Appl. Phys. Lett. **123**, 032404 (2023); doi: 10.1063/5.0153329
Submitted: 6 April 2023 · Accepted: 1 July 2023 ·
Published Online: 18 July 2023

Biswajit Sahoo,[1,2,a)] Alex Frano,[1,2] and Eric. E. Fullerton[1]

AFFILIATIONS

[1]Center for Memory and Recording Research, University of California, San Diego, 9500 Gilman Dr, La Jolla, California 92093-0401, USA
[2]Department of Physics, University of California, San Diego, 9500 Gilman Dr, La Jolla, California 92093-0401, USA

[a)]Author to whom correspondence should be addressed: bsahoo@ucsd.edu

ABSTRACT

Many 5d transition metal oxides have a unique electronic structure, where the density of states near the Fermi level is dominated by only 5d electrons with strong spin–orbit coupling. IrO_2, a Dirac nodal line semi-metal, is the simplest of these oxides. The presence of 5d electrons and gap opening of Dirac nodal lines via strong spin–orbit coupling allows for the hybridization of the 5d electrons of the oxide with the itinerant d electrons of a ferromagnet, while simultaneously increasing the intrinsic spin Hall effect. We report large charge-to-spin conversion in thin films of this material using spin-torque ferromagnetic resonance experiments. By independently performing line shape analysis and linewidth modulation experiments, we conclusively determine the spin Hall angle of optimized IrO_2 films to be ∼8 times larger than that of Pt.

Spintronics, electronics that employ the spin of an electron instead of (or in addition to) its charge, has found extensive applications in data storage[1] and nonvolatile magnetic random access memories (MRAM).[2,3] In these applications, the spin current is generated by passing the electric current through a ferromagnetic layer where the current becomes spin polarized. New applications, such as spin–orbit torque (SOT) MRAM,[4,5] field free spin–orbit torque switching,[6] or SOT oscillators,[7] exploit spin-currents generated from charge currents in a non-magnetic layer via the spin Hall effect (SHE).[8–10] SHE stems from the relativistic spin–orbit coupling (SOC) of a material that generates a transverse spin current from a conventional charge current.[11] Designing materials with a large SHE will allow the development of new classes of energy efficient nonvolatile memories,[12] logic devices, and neuromorphic computing approaches.[13]

Spin Hall angle (SHA) is a measure of the efficiency of a material to convert the charge current to spin current and is the figure of merit for materials to be used in spintronic devices. As SOC is proportional to Z^4 (Z being the atomic number), heavy metals, such as Pt,[14] Pd,[15] W,[16] and beta-Ta,[17] are popularly used to generate spin currents from charge currents. The density of states in these materials near the Fermi level is dominated by both 5d and 6s electrons. In contrast, 5d transition metal oxides have a unique electronic structure where the density of states near the Fermi level is dominated only by 5d electrons with strong SOC.[18] IrO_2, the simplest of these oxides, is predicted to host networks of type-1 Dirac nodal lines. In the presence of strong SOC, it is predicted that gaps open in the hexatruple and octuple points of these networks, leading to large intrinsic SHE.[19] Experimentally, researchers have explored IrO_2 for its efficacy as a spin current detector with SHA of 0.065[20] or as a spin current generator with SHA of 0.095 to 0.26 using a variety of measurement techniques.[21,22] In this Letter, we measure spin torque ferromagnetic resonance (ST-FMR) on optimized polycrystalline IrO_2-CoFeB bilayers to quantify the effect of the spin–orbit torques on the magnetization dynamics of the ferromagnet (FM) and subsequently determine the SHA of IrO_2. Till date line shape analysis via ST-FMR has been performed on epitaxial (001) IrO_2[23] with an SHA of 0.45 at room temperature. However, no such report exists for polycrystalline IrO_2. We use both line shape analysis and linewidth modulation to independently quantify the SHA in IrO_2. Furthermore, we performed the same experiments on a Pt-CoFeB bilayer to compare the SHA of Pt and polycrystalline IrO_2.

IrO_2 thin films were grown onto oxidized Si (100) substrates with a 300-nm amorphous SiO_2 layer in high vacuum with base pressure better than 1.0×10^{-7} Torr. The FM used was $Co_{40}Fe_{40}B_{20}$ (CoFeB). The samples fabricated are substrate/IrO_2(x)/$Co_{40}Fe_{40}B_{20}$(7)/SiO_2(5) (the numbers in parentheses represent the thicknesses in nm), where x= 3, 5, 7, 10, or 20 nm, and these samples are named S1–S5,

respectively. During fabrication, the substrate was rotated uniformly at 20 rpm during the deposition of all the layers. The optimized deposition parameters for the samples are described as follows: IrO_2 films were reactively sputtered at room temperature from a 99.99% pure Ir target at a rate of 0.028 nm/s. The total deposition pressure of Ar and O_2 (Ar:O_2: : 2:1) was kept constant at 2.5 mTorr. The films were then annealed at 700 ° C pressure for 15 min in an oxygen atmosphere of 25 mTorr in the deposition chamber. After cooldown in vacuum, CoFeB layers were deposited *in situ* at a rate of 0.034 nm/s at 2.5 mTorr Ar pressure. The films were then capped with 5-nm thick SiO_2 capping layers to prevent the oxidation of the CoFeB. We further fabricated an IrO_2 layer at 700 ° C to compare with the annealed sample. We fabricated a sample (S0) of substrate/CoFeB (7)/Pt (5) at room temperature. The deposition rate for Pt is 0.04 nm/s. The Pt serves both as a capping layer and the heavy metal (HM) layer. We also deposit CoFeB(7)/SiO_2(5) as a reference sample (S6).

Single layers of CoFeB (7), IrO_2(20), and Pt (5) were grown for resistivity measurements using the van der Pauw method. The resistivities for CoFeB and Pt were found to be 120 and 26 μΩ cm, respectively. The resistivity of unannealed IrO_2 deposited at room temperature was 356 μΩ cm, while that of IrO_2 deposited at room temperature and annealed at 700 ° C was 142 μΩ cm. The resistivity of IrO_2 grown at 700 ° C was 57 μΩ cm. X-ray reflectivity (XRR) and x-ray diffraction (XRD) were performed on annealed and unannealed thin films (Fig. 1) using a Rigaku SmartLab system using Cu-K_α x rays. The XRR fringes are deep and well defined, which qualitatively indicate that the IrO_2 films were smooth. The XRR spectra were fitted using the Parratt recursion formalism to reveal a surface roughness of 0.6 nm for unannealed and 0.3 nm for annealed thin films. Further, XRD spectra [Fig. 1(a)] showed that the annealed IrO_2 film was polycrystalline with (110), (101), and (200) crystal orientations. For comparison, the IrO_2 film grown at 700 ° C had a surface roughness >4 nm as obtained from atomic force microscopy measurements [supplementary Fig. S1(b)]. Since a low roughness and low resistivity are crucial for the formation of sharp interfaces and significant current flow through the high SOC layer, we used the post-annealed polycrystalline IrO_2 films in the subsequent experiments.

ST-FMR is a robust technique to probe the charge to spin conversion (J_s/J_c) efficiency of materials, where J_s and J_c are the spin current density and charge current density, respectively. The devices for ST-FMR were fabricated by photolithography. First, coplanar waveguide channels of 10 × 20 μm^2 dimensions were patterned and milled

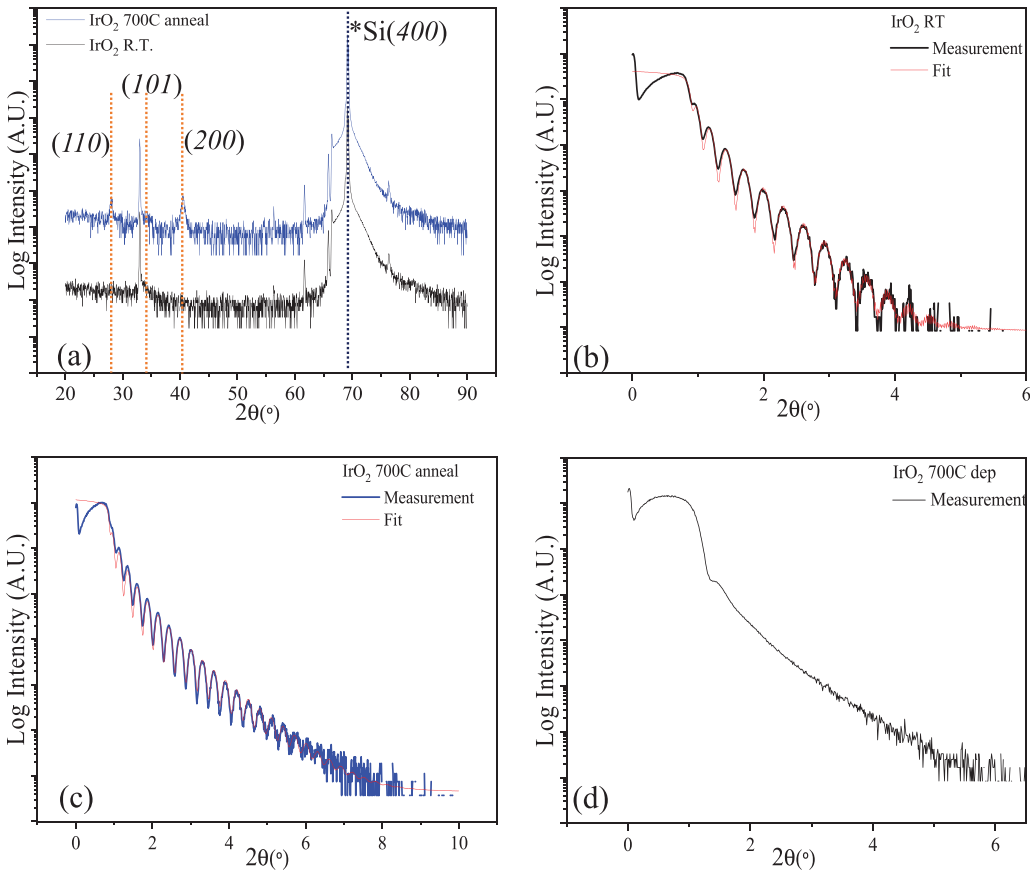

FIG. 1. (a) The XRD spectra of annealed (top) and room temperature (bottom) growth of 20 nm IrO_2 films. The top spectra show distinct IrO_2 peaks: (110), (101), and (200). (b) The XRR spectra of room temperature grown sample, with a roughness of 0.63 nm. The annealed sample (c) has a roughness of 0.34 nm. When deposited at a substrate temperature of 700 °C, the surface had more roughness (>4 nm) as shown from the XRR data in (d).

using Ar ion. Next, Ti (70)/Au (200) electrode pads were fabricated using magnetron sputtering and lift-off. The symmetric ground-signal-ground (G-S-G) configuration was used to minimize the z-component of the radio frequency (RF) field.[24] The device was then wire bonded by gold wires onto transmission lines to provide an RF current into the system (Fig. 2). The device was positioned at 45° angle with respect to the in-plane external field to improve the magnitude of the ST-FMR signal.[24] When an RF current (I_{RF}) flows through a material [generally a non-magnet (NM)] with high SOC, transverse non-equilibrium spins are generated, which propagate into the FM. The resulting SOT acting on the FM is oscillatory in nature and results in the precession of the FM that is detected via the anisotropic magnetoresistance (AMR) of the FM. The injected I_{RF} combined with the oscillating AMR results in the generation of a DC mixing voltage (V_{mix}), which is detected by a lock-in amplifier after being filtered through a bias tee. The signal magnitude becomes maximum under the condition of ferromagnetic resonance. The resulting V_{mix} consists of a symmetric (V_S) and an anti-symmetric (V_A) component, which is fit by the following equation:[25]

$$V_{mix} = V_S \frac{(\Delta H/2)^2}{(H - H_0)^2 + (\Delta H/2)^2} + V_A \frac{((\Delta H/2)(H - H_0))}{(H - H_0)^2 + (\Delta H/2)^2} + \text{background}. \quad (1)$$

Here, ΔH is the linewidth, H is the applied field, and H_0 is the resonant field. The symmetric part of the signal is due to the spin currents, whereas the anti-symmetric part is mainly due to the stray oersted fields. From the ratio of V_S and V_A, the SHA can be calculated using the following expression:[14]

$$\frac{J_{S,rf}}{J_{C,rf}} = \frac{S}{A}\frac{(e\mu_0 M_s t d)}{\hbar}\left[1 + \left(\frac{4\pi M_{eff}}{H_0}\right)\right]^{\frac{1}{2}}. \quad (2)$$

Here, S and A represent the symmetric and anti-symmetric component of the V_{mix}, respectively, and M_s is the saturation magnetization. t and d refer to the thickness of IrO_2 and CoFeB, respectively. e is the electronic charge, and μ_0 is the relative permeability of free space. M_{eff} is the effective magnetization (622 and 700 Oe for S5 and S0, respectively). The reduced value in S5 may have been due to the oxidation/formation of a thin dead layer between IrO_2 and CoFeB.[22] To determine the approximate thickness of the FM layer in S5, we perform magnetometry measurements on samples S6 and S5 (supplementary Fig. S2) and determine the saturation magnetization per unit area (M_sd) for these films. M_sd depends linearly on the thickness,[26] and from this, the thickness of CoFeB in S5 was found to be 6.03 nm. Consequently, we determine M_s, which is 1028 and 1032 emu/cc for S5 and S0, respectively.

Using Eq. (2), we average over several frequencies ranging from 5 to 10 GHz and find the SHA of Pt to be 0.07 ± 0.01 (not shown), comparable with previous findings.[24,27,28] We perform line shape ST-FMR experiments for samples S1–S5 and find that the SHA for IrO_2 saturates around 0.31 ± 0.03, for 20 nm IrO_2 [Fig. 3(d)], a fourfold increase than that of Pt. The increase in SHA with thickness of IrO_2 may be due to the reduction in the resistance of the IrO_2 layer, which results in a higher current flow and hence larger SOTs on the CoFeB layer. Additionally, the polycrystalline nature of IrO_2 may be aiding in a higher spin scattering, resulting in higher signal values. Another reason for the increase in the SHA may be due to the preservation of the S/A ratio (S/A ≈ 0.3) in the ST-FMR signal in our case, which normally decreases with the thickness of HM-FM layers.[14] It is possible that due to the higher spin diffusion length or proper interface conditions, the S/A ratio remains preserved in IrO_2-CoFeB bilayers despite the higher thickness of IrO_2. To further investigate the interfacial conditions in sample S5, we estimated the effective spin mixing conductance (g_{eff}) and the spin interface transparency (T).

To determine T, we need the spin diffusion length of IrO_2 (λ_{IrO_2}). λ_{IrO_2} is obtained from the IrO_2 thickness vs SHA plot after fitting by the following phenomenological equation:[29]

$$\eta = \eta_1\left(1 - \text{sech}\left(\frac{t_{IrO_2}}{\lambda_{IrO_2}}\right)\right). \quad (3)$$

Here, η is the SHA, and η_1 is the saturation SHA of the NM. From the fitting, we find the spin diffusion length of IrO_2 to be of 4.3 ± 0.5 nm

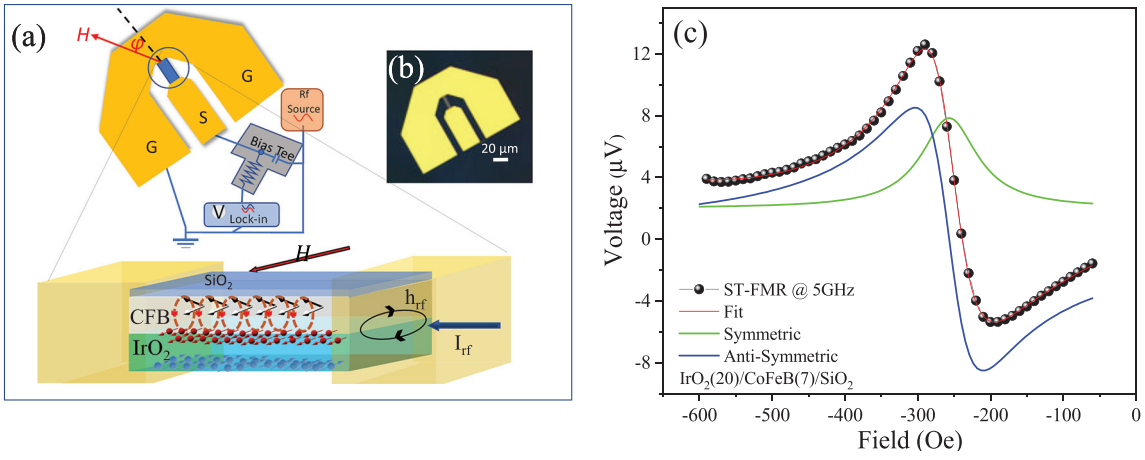

FIG. 2. (a) The device setup with a zoomed-in view of the sample structure and RF fields. (b) The light microscope image of the device. The sample under consideration is 10 × 20 μm^2. The angle φ is 45°. (c) The ST-FMR spectra at 5 GHz and a decomposition into the symmetric and anti-symmetric components.

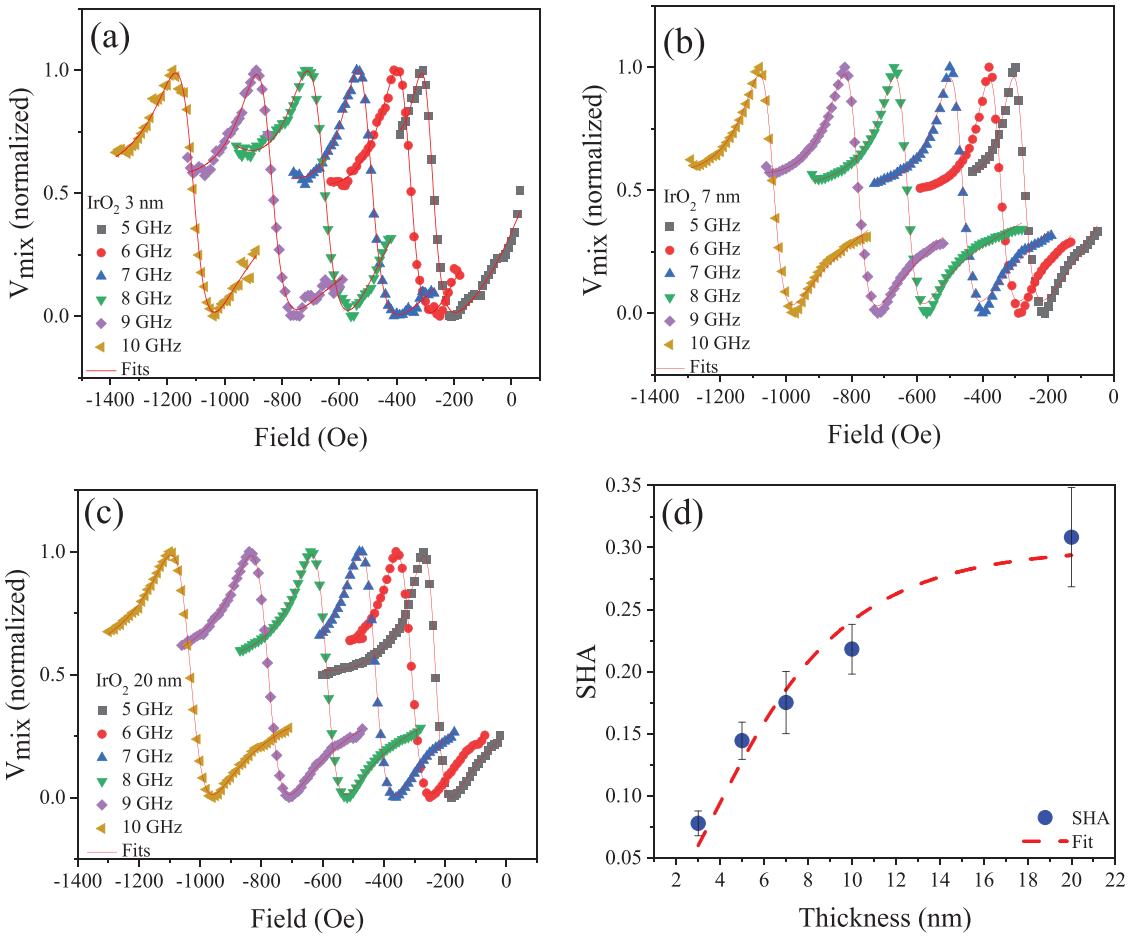

FIG. 3. (a)–(c) The ST-FMR spectra at different frequencies for IrO_2 thickness of 3, 7, and 20 nm, respectively. (d) The plot of the obtained spin Hall angle vs thickness of IrO_2 with the fitting (dashed line) as per Eq. (3).

with saturation SHA of 0.30 ± 0.02. The SHA agrees closely to that obtained by the line shape method. Additionally, the value of λ_{IrO_2} for poly-crystalline IrO_2 is slightly higher than that reported in the literature.[20,30]

The g_{eff} for S5 is found by the following equation:[29]

$$g_{eff} = \frac{4\pi M_s d \Delta\alpha}{g\mu_B}. \quad (4)$$

Here, g is the Lande g factor, μ_B is the Bohr magneton, and Δa is the difference between Gilbert damping of S5 (0.028 609) and S6 (0.008). The spin mixing conductance provides a measure of the efficiency of transmission of spins through the interface and has a value of $8.2 \times 10^{19}\ m^{-2}$ for S5. This value is higher than that reported in Pt systems.[31–33] Finally, we calculate T from using the following equation:[34]

$$T = \frac{g_r \tanh\left(\frac{t_{IrO_2}}{\lambda_{IrO_2}}\right)}{g_r \coth\left(\frac{t_{IrO_2}}{\lambda_{IrO_2}}\right) + \frac{h}{2e^2 \rho_{IrO_2} \lambda_{IrO_2}}}. \quad (5)$$

Here, g_r is the real part of g_{eff}. We have assumed $g_r = g_{eff}$ in our calculations. h is the Planck's constant, and ρ_{IrO2} is the resistivity of IrO_2. The value of T determines the level of electronic structure matching between the FM and NM layers. The spin interface transparency for S5 is found to be around 95%. High values of g_{eff} and T indicate efficient spin transmission in the FM-NM interface.

It is to be noted that line shape analysis method has some limitations. While using Eq. (2), we assume that the field-like torque contribution, which can arise from interfacial effects, such as the Rashba effect, is minimum. Since field-like torques also produce an antisymmetric voltage, the value of SHA may be over- or under-estimated.[35,36] To confirm that the SHA of IrO_2 is indeed large, we also performed DC-current bias ST-FMR measurements. This technique, also known as the modulation of linewidth, involves injection of a biasing DC current in addition to the RF current. Due to the DC current, a static anti-damping like torque modulates the damping of the FM, effectively modulating the linewidth.[25] The injected DC current can increase (decrease) the linewidth if the spin polarization is parallel (anti-parallel) to the FM magnetization.[14] Since this technique is a bipolar measurement, where the DC current systematically changes

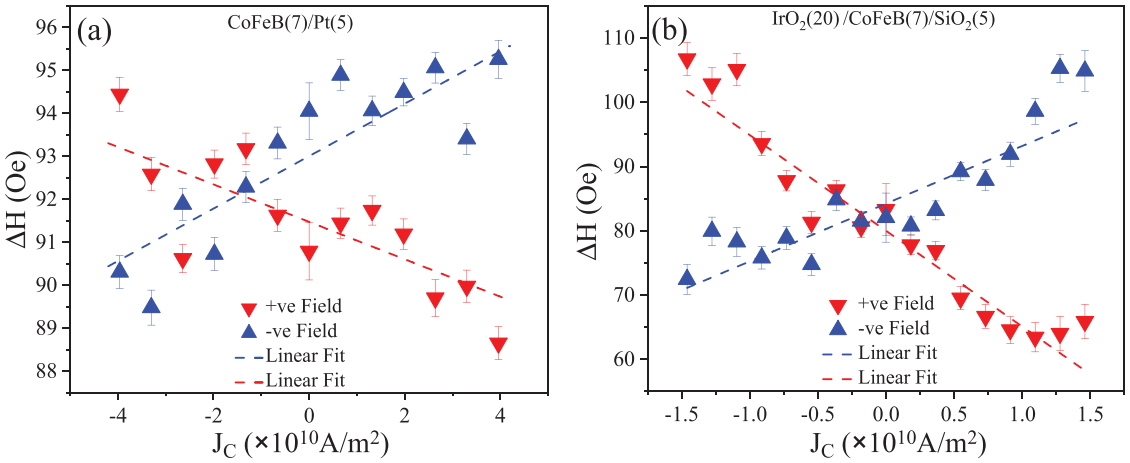

FIG. 4. DC bias linewidth modulation at 8 GHz r.f. for (a) CFB (7)/Pt (5) and (b) IrO_2(20)/CFB(7)/SiO_2(5) systems. The slope of the IrO_2 system is higher than that of Pt showing higher SHA in 20 nm IrO_2.

the linewidth in an opposite manner for positive and negative fields, one can determine the SOT generated by the material under consideration. Further, additional effects due to the inverse spin Hall effect are eliminated in this technique. The SHA can be determined from the slope of the linewidth vs current density plot using the following equation:[37]

$$\frac{J_S}{J_C} = \frac{\gamma e\left(H_0 + \frac{M_{eff}}{2}\right)\mu_0 M_s t}{2\pi f \sin(\phi)} \frac{d\Delta}{dJ_C}. \quad (6)$$

Here, γ is the gyromagnetic ratio, f is the applied frequency, ϕ is the angle between direction of I_{RF} and external magnetic field (45°), and $d\Delta/dJ_c$ is the slope of the linewidth-current density plot. All other parameters have been described previously.

In Figs. 4(a) and 4(b), the results from the modulation of linewidth technique are shown for S0 and S5, respectively. The SHA values obtained are 0.04 ± 0.01 for Pt and 0.36 ± 0.07 for IrO_2.

From the two techniques, we can conclusively determine that the SHA of polycrystalline IrO_2 is much larger than Pt. The SHA for IrO_2 obtained from the linewidth modulation is in close agreement with that obtained by the line shape method, albeit with a slightly higher error margin. One of the reasons for this could be the linewidth broadening due to thermal effects at higher current densities, which can result in non-linearities in the otherwise linear linewidth vs current behavior. From the phenomenological fit [Eq. (3)], we note that the saturation SHA of IrO_2 to be 0.30 ± 0.02. However, from the linewidth dependence, we find the value of SHA of 20 nm IrO_2 to be 0.36 ± 0.07. This indicates that apart from intrinsic, there seems to be a role of extrinsic contributions as well. While we cannot exactly quantify the extrinsic effects contribution to the SHA, we can say that the proper interfacial conditions in our sample may have played an important role in maximizing the SHA. This is exemplified by our calculations of g_{eff} and T for S5. High values of geff and T indicate the efficient transmission of spins and proper electronic structure matching between the CoFeB and IrO_2 layers. Due to this, the effect of the SOTs on the FM generated by the charge to spin conversion of the DC current may have been more pronounced leading to higher modulation of linewidth. We note that despite the thermal effects, the change in linewidth with the applied current is significant for IrO_2. This is exemplified by the high SHA of IrO_2, which is around eight times higher than Pt in the linewidth analysis method.

The room temperature ST-FMR analysis shows a very high SHA of polycrystalline IrO_2, which is higher than previously reported values using different measurement techniques: SHA = 0.26 via the inverse spin Hall effect,[22] second harmonic Hall resistance SHA = 0.095,[21] or non-local spin valve measurements SHA = 0.065.[20] The optimization of the IrO_2 roughness and conductivity may have contributed to the observed high SHA values. Vacuum annealing the IrO_2 resulted in a better connectivity between the individual grains, thereby increasing the conductivity.[38] The film roughness was further optimized to be better than 0.4 nm. High conductivity would result in a large current flow in the IrO_2 layer and consequently higher spin currents, while the smooth interfacial conditions would facilitate the efficient transmission of spins into the FM, resulting in higher SOTs. From the DC current bias study, we can extrapolate the critical current density (J_c) required to achieve zero linewidth. For IrO_2, $J_{c\text{-critical}}$ is $\approx 1.2 \times 10^{11}$ A/m^2. Current densities higher than this will generate auto-oscillations. This critical current value is significantly lower than reported J_c values required by heavy metals for auto-oscillation in spin Hall nano-oscillators,[39,40] making IrO_2 an attractive candidate for use in oscillator applications.

In summary, optimized polycrystalline IrO_2 has conclusively shown a high SHA consistent with its high Z and theoretical predictions. High SHA and large conductivity of IrO_2 may have implications for use in the development of all oxide-based energy efficient spintronic devices and for applications, such as nano-oscillators and magnetic switching, where one can interface IrO_2 with low damping ferromagnetic oxides to achieve new spintronic functionalities.

See the supplementary material for data of magnetometry and surface morphology measurements.

This collaborative work was supported as a part of Quantum Materials for Energy Efficient Neuromorphic Computing

(Q-MEEN-C), an Energy Frontier Research Center funded by the U.S. Department of Energy (DOE), Office of Science, Basic Energy Sciences (BES), under Award No. DE-SC0019273. This work was also performed in part at the San Diego Nanotechnology Infrastructure (SDNI) of UCSD, a member of the National Nanotechnology Coordinated Infrastructure, which is supported by the National Science Foundation (Grant ECCS-2025752).

AUTHOR DECLARATIONS

Conflict of Interest

The authors have no conflicts to disclose.

Author Contributions

Biswajit Sahoo: Data curation (lead); Formal analysis (lead); Investigation (equal); Visualization (lead); Writing – original draft (lead); Writing – review & editing (supporting). **Alex Frano:** Conceptualization (equal); Funding acquisition (lead); Investigation (equal); Resources (lead); Supervision (equal); Validation (equal); Writing – original draft (equal); Writing – review & editing (lead). **Eric Fullerton:** Conceptualization (lead); Funding acquisition (lead); Investigation (equal); Methodology (equal); Project administration (lead); Resources (lead); Supervision (equal); Validation (equal); Writing – original draft (equal); Writing – review & editing (lead).

DATA AVAILABILITY

The data that support the findings of this study are available from the corresponding author upon reasonable request.

REFERENCES

[1]E. E. Fullerton and J. R. Childress, "Spintronics, magnetoresistive heads, and the emergence of the digital world," Proc. IEEE **104**, 1787–1795 (2016).
[2]D. Apalkov, B. Dieny, and J. M. Slaughter, "Magnetoresistive random access memory," Proc. IEEE **104**, 1796–1830 (2016).
[3]R. Sbiaa and S. N. Piramanayagam, "Recent developments in spin transfer torque MRAM," Phys. Status Solidi RRL **11**, 1700163 (2017).
[4]S.-W. Lee and K.-J. Lee, "Emerging three-terminal magnetic memory devices," Proc. IEEE **104**, 1831–1843 (2016).
[5]K. Garello, F. Yasin, and G. S. Kar, "Spin-orbit torque MRAM for ultrafast embedded memories: From fundamentals to large scale technology integration," in Proceedings of IEEE 11th International Memory Workshop (IMW), Monterey, CA, 2019.
[6]Y.-C. Lau, D. Betto, K. Rode, J. M. D. Coey, and P. Stamenov, "Spin–orbit torque switching without an external field using interlayer exchange coupling," Nat. Nanotechnol. **11**, 758–762 (2016).
[7]J.-R. Chen, A. Smith, E. A. Montoya, J. G. Lu, and I. N. Krivorotov, "Spin–orbit torque nano-oscillator with giant magnetoresistance readout," Commun. Phys. **3**, 187 (2020).
[8]M. I. Dyakonov and V. I. Perel, "Current-induced spin orientation of electrons in semiconductors," Phys. Lett. A **35**, 459–460 (1971).
[9]J. E. Hirsch, "Spin Hall effect," Phys. Rev. Lett. **83**, 1834–1837 (1999).
[10]J. Sinova, S. O. Valenzuela, J. Wunderlich, C. Back, and T. Jungwirth, "Spin Hall effects," Rev. Mod. Phys. **87**, 1213–1260 (2015).
[11]F. Hellman, A. Hoffmann, Y. Tserkovnyak, G. S. Beach, E. E. Fullerton, C. Leighton, A. H. MacDonald, D. C. Ralph, D. A. Arena, H. A. Dürr, P. Fischer, J. Grollier, J. P. Heremans, T. Jungwirth, A. V. Kimel, B. Koopmans, IN. Krivorotov, S. J. May, A. K. Petford-Long, J. M. Rondinelli, N. Samarth, I. K. Schuller, A. N. Slavin, M. D. Stiles, O. Tchernyshyov, A. Thiaville, and B. L. Zink, "Interface-induced phenomena in magnetism," Rev. Mod. Phys. **89**, 025006 (2017).
[12]S. K. Thirumala, S. Jain, A. Raghunathan, and S. K. Gupta, "Non-volatile memory utilizing reconfigurable ferroelectric transistors to enable differential read and energy-efficient in-memory computation," in Proceedings of 2019 IEEE/ACM International Symposium on Low Power Electronics and Design (ISLPED), Lausanne, Switzerland, 2019.
[13]J. Grollier, D. Querlioz, K. Y. Camsari, K. Everschor-Sitte, S. Fukami, and M. D. Stiles, "Neuromorphic spintronics," Nat. Electron. **3**, 360–370 (2020).
[14]L. Liu, T. Moriyama, D. C. Ralph, and R. A. Buhrman, "Spin-torque ferromagnetic resonance induced by the spin Hall effect," Phys. Rev. Lett. **106**, 036601 (2011).
[15]K. Ando and E. Saitoh, "Inverse spin-Hall effect in palladium at room temperature," J. Appl. Phys. **108**, 113925 (2010).
[16]C.-F. Pai, L. Liu, Y. Li, H. W. Tseng, D. C. Ralph, and R. A. Buhrman, "Spin transfer torque devices utilizing the giant spin Hall effect of tungsten," Appl. Phys. Lett. **101**, 122404 (2012).
[17]J. Kim, J. Sinha, M. Hayashi, M. Yamanouchi, S. Fukami, T. Suzuki, S. Mitani, and H. Ohno, "Layer thickness dependence of the current-induced effective field vector in Ta|CoFeB|MgO," Nat. Mater. **12**, 240–245 (2013).
[18]Y. Ping, G. Galli, and W. A. Goddard, "Electronic structure of IrO_2: The role of the metal d orbitals," J. Phys. Chem. C **119**, 11570–11577 (2015).
[19]Y. Sun, Y. Zhang, C.-X. Liu, C. Felser, and B. Yan, "Dirac nodal lines and induced spin Hall effect in metallic rutile oxides," Phys. Rev. B **95**, 235104 (2017).
[20]K. Fujiwara, Y. Fukuma, J. Matsuno, H. Idzuchi, Y. Niimi, Y. Otani, and H. Takagi, "5*d* iridium oxide as a material for spin-current detection," Nat. Commun. **4**, 2893 (2013).
[21]K. Ueda, N. Moriuchi, K. Fukushima, T. Kida, M. Hagiwara, and J. Matsuno, "Spin-orbit torque generation in NiFe/IrO_2 bilayers," Phys. Rev. B **102**(13), 134432 (2020).
[22]B. Sahoo, K. Roy, P. Gupta, A. Mishra, B. Satpati, B. B. Singh, and S. Bedanta, "Spin pumping and inverse spin Hall effect in iridium oxide," Adv. Quantum Technol. **4**, 2000146 (2021).
[23]A. Bose, J. N. Nelson, X. S. Zhang, P. Jadaun, R. Jain, D. G. Schlom, D. C. Ralph, D. A. Muller, K. M. Shen, and R. A. Buhrman, "Effects of anisotropic strain on spin–orbit torque produced by the Dirac nodal line semimetal IrO_2," ACS Appl. Mater. Interfaces **12**, 55411–55416 (2020).
[24]Y. Wang, P. Deorani, X. Qiu, J. H. Kwon, and H. Yang, "Determination of intrinsic spin Hall angle in Pt," Appl. Phys. Lett. **105**, 152412 (2014).
[25]J. C. Slonczewski, "Current-driven excitation of magnetic multilayers," J. Magn. Magn. Mater. **159**, L1–L7 (1996).
[26]M. Belmeguenai, M. S. Gabor, Y. Roussigne, F. Zighem, S. M. Cherif, and C. Tiusan, "Perpendicular magnetic anisotropy in Co_2 FeAl thin films: Effect of annealing temperature," IEEE Trans. Magn. **51**, 6000803 (2015).
[27]S. Keller, L. Mihalceanu, M. R. Schweizer, P. Lang, B. Heinz, M. Geilen, T. Brächer, P. Pirro, T. Meyer, A. Conca, D. Karfaridis, G. Vourlias, T. Kehagias, B. Hillebrands, and E. T. Papaioannou, "Determination of the spin Hall angle in single-crystalline Pt films from spin pumping experiments," New J. Phys. **20**, 053002 (2018).
[28]Y. Xiao, H. Wang, and E. E. Fullerton, "Crystalline orientation–dependent spin Hall effect in epitaxial platinum," Front. Phys. **9**, 791736 (2022).
[29]Y. Tserkovnyak, A. Brataas, G. E. W. Bauer, and B. I. Halperin, "Nonlocal magnetization dynamics in ferromagnetic heterostructures," Rev. Mod. Phys. **77**, 1375–1421 (2005).
[30]P. Jiménez-Cavero, I. Lucas, J. Ara-Arteaga, M. R. Ibarra, P. A. Algarabel, and L. Morellón, "Strong crystallographic influence on spin Hall mechanism in PLD-grown IrO_2 thin films," Nanomaterials **11**, 1478 (2021).
[31]O. Mosendz, J. E. Pearson, F. Y. Fradin, G. E. W. Bauer, S. D. Bader, and A. Hoffmann, "Quantifying spin Hall angles from spin pumping: Experiments and theory," Phys. Rev. Lett. **104**, 046601 (2010).
[32]S. Mizukami, Y. Ando, and T. Miyazaki, "Effect of spin diffusion on Gilbert damping for a very thin permalloy layer in Cu/permalloy/Cu/Pt films," Phys. Rev. B **66**, 104413 (2002).
[33]Y. Tserkovnyak, A. Brataas, and G. E. W. Bauer, "Spin pumping and magnetization dynamics in metallic multilayers," Phys. Rev. B **66**, 224403 (2002).
[34]W. Zhang, W. Han, X. Jiang, S.-H. Yang, and S. S. P. Parkin, "Role of transparency of platinum–ferromagnet interfaces in determining the intrinsic magnitude of the spin Hall effect," Nat. Phys. **11**, 496–502 (2015).

[35]G. Allen, S. Manipatruni, D. E. Nikonov, M. Doczy, and I. A. Young, "Experimental demonstration of the coexistence of spin Hall and Rashba effects in β-tantalum/ferromagnet bilayers," Phys. Rev. B **91**, 144412 (2015).
[36]T. D. Skinner, M. Wang, A. T. Hindmarch, A. W. Rushforth, A. C. Irvine, D. Heiss, H. Kurebayashi, and A. J. Ferguson, "Spin-orbit torque opposing the Oersted torque in ultrathin Co/Pt bilayers," Appl. Phys. Lett. **104**, 062401 (2014).
[37]W. Zhang, M. B. Jungfleisch, F. Freimuth, W. Jiang, J. Sklenar, J. E. Pearson, J. B. Ketterson, Y. Mokrousov, and A. Hoffmann, "All-electrical manipulation of magnetization dynamics in a ferromagnet by antiferromagnets with anisotropic spin Hall effects," Phys. Rev. B **92**, 144405 (2015).
[38]G. Lodi, A. D. Battisti, G. Bordin, C. D. Asmundis, and A. Benedetti, "Microstructure and electrical properties of IrO_2 prepared by thermal decomposition of $IrCl_3{\cdot}x$ H_2O: Role played by the conditions of thermal treatment," J. Electroanal. Chem. Interfacial Electrochemistry **277**, 139–150 (1990).
[39]V. E. Demidov, S. Urazhdin, H. Ulrichs, V. Tiberkevich, A. Slavin, D. Baither, G. Schmitz, and S. O. Demokritov, "Magnetic nano-oscillator driven by pure spin current," Nat. Mater. **11**, 1028–1031 (2012).
[40]M. Ranjbar, P. Durrenfeld, M. Haidar, E. Iacocca, M. Balinskiy, T. Q. Le, M. Fazlali, A. Houshang, A. A. Awad, R. K. Dumas, and J. Akerman, "CoFeB-based spin Hall nano-oscillators," IEEE Magn. Lett. **5**, 1–4 (2014).